

GA-A25840

**BROAD WAVENUMBER TURBULENCE AND  
TRANSPORT DURING LOW POWER ELECTRON  
CYCLOTRON HEATING IN THE DIII-D TOKAMAK**

by

**T.L. RHODES, W.A. PEEBLES, J.C. DeBOO, R. PRATER, J.E. KINSEY,  
G.M. STAEBLER, J. CANDY, M.E. AUSTIN, R.V. BRAVENEC, K.H. BURRELL,  
J.S. deGRASSIE, E.J. DOYLE, P. GOHIL, C.M. GREENFIELD, R.J. GROEBNER,  
J. LOHR, M.A. MAKOWSKI, X.V. NGUYEN, C.C. PETTY, W.M. SOLOMON,  
H.E. ST JOHN, M.A. VAN ZEELAND, G. WANG, and L. ZENG**

**JULY 2007**



## **DISCLAIMER**

This report was prepared as an account of work sponsored by an agency of the United States Government. Neither the United States Government nor any agency thereof, nor any of their employees, makes any warranty, express or implied, or assumes any legal liability or responsibility for the accuracy, completeness, or usefulness of any information, apparatus, product, or process disclosed, or represents that its use would not infringe privately owned rights. Reference herein to any specific commercial product, process, or service by trade name, trademark, manufacturer, or otherwise, does not necessarily constitute or imply its endorsement, recommendation, or favoring by the United States Government or any agency thereof. The views and opinions of authors expressed herein do not necessarily state or reflect those of the United States Government or any agency thereof.

# BROAD WAVENUMBER TURBULENCE AND TRANSPORT DURING LOW POWER ELECTRON CYCLOTRON HEATING IN THE DIII-D TOKAMAK

by

T.L. RHODES,\* W.A. PEEBLES,\* J.C. DeBOO, R. PRATER, J.E. KINSEY,  
G.M. STAEBLER, J. CANDY, M.E. AUSTIN,† R.V. BRAVENEC,† K.H. BURRELL,  
J.S. deGRASSIE, E.J. DOYLE,\* P. GOHIL, C.M. GREENFIELD, R.J. GROEBNER,  
J. LOHR, M.A. MAKOWSKI,‡ X.V. NGUYEN,\* C.C. PETTY, W.M. SOLOMON,#  
H.E. ST JOHN, M.A. VAN ZEELAND, G. WANG,\* and L. ZENG\*

This is a preprint of an invited paper to be presented at the 34th  
EPS Conf. on Plasma Physics, in Warsaw, Poland, July 2-7, 2007  
and to be published in the *Plasma Phys. Control. Fusion*.

\*University of California-Los Angeles, Los Angeles, California.

†University of Texas-Austin, Austin, Texas.

‡Lawrence Livermore National Laboratory, Livermore, California.

#Princeton Plasma Physics Laboratory, Princeton, New Jersey.

Work supported by  
the U.S. Department of Energy  
under DE-FG03-01ER54615, DE-FC02-04ER54698, DE-FG03-97ER54415,  
W-7405-ENG-48, and DE-AC02-76CH03073

GENERAL ATOMICS PROJECT 30200  
JULY 2007



## Abstract

The response of plasma parameters and broad wavenumber turbulence ( $1\text{--}39\text{ cm}^{-1}$ ,  $k\rho_s = 0.1\text{--}10$ , relevant to ion temperature gradient, trapped electron mode, and electron temperature gradient mode turbulence, here  $\rho_s =$  ion gyroradius) to auxiliary electron cyclotron heating (ECH) is reported on. One fluid thermal fluxes and diffusivities increase appreciably with ECH. Significant changes to the density fluctuations over the full range of measured wavenumbers are observed, with an increase for lower wavenumbers and a more spatially complicated response at high  $k$ . Spatially resolved high  $k$  measurements ( $k = 39\text{ cm}^{-1}$ ,  $k\rho_s = 4\text{--}10$ ) show a varying response to ECH, with  $\tilde{n}$  decreasing at  $r/a = 0.35$  and increasing at  $r/a = 0.6$  and  $1$ . These variations were found to have a positive correlation with  $\nabla T_e$  evaluated at nearby locations, consistent with a  $\nabla T_e$  drive. Comparison of the changes in high  $k$  fluctuation levels to linear gyrokinetic growth rates show qualitative agreement at the innermost location,  $r/a = 0.35$  and disagreement at  $r/a = 0.6$ .



## 1. Introduction

Anomalous electron heat transport is an important and unresolved issue that directly impacts the understanding and prediction of fusion reactor performance [1,2]. Although lower wavenumber turbulence and resulting transport are thought to be fairly well understood [1,2], the interaction of low, intermediate, and high- $k$  fluctuations and their combined impact on transport is a potentially complex system that calls for measurements over a broad wavenumber range [3-5]. Turbulence measurements over a range in wavenumbers have been undertaken on a variety of fusion research devices. These efforts generally employ some type of scattering to access the higher wavenumber range of interest, including far infrared (FIR) forward scattering and mm-wave backscattering in DIII-D [6,7], enhanced upper-hybrid resonance backscattering in FT-2 [8,9], far-forward FIR scattering in Tore-Supra [10], to FIR forward scattering in NSTX [9]. These efforts have reported density fluctuations over a large range in wavenumber corresponding to low- $k$  ion temperature gradient instability (ITG) ( $k\rho_s \lesssim 0.5$ ), trapped electron mode instability (TEM) ( $k\rho_s \lesssim 2$ ), up to and including high- $k$  electron temperature gradient instability (ETG) ( $k\rho_s > 2$ ) (these  $k\rho_s$  ranges are only approximate,  $\rho_s$  is the ion gyroradius evaluated using the electron temperature). The question of how much transport can be attributed to high- $k$ , ETG type modes is currently an unresolved question. Since these modes can interact with, and perhaps be driven by, the lower  $k$  fluctuations it is important to measure the turbulence over as broad a range as possible. In this regard, work on DIII-D indicates that the high  $k$  ETG scale fluctuations can evolve independently of lower  $k$  fluctuations in some cases [7].

In this paper the effects of electron cyclotron heating (ECH) upon Ohmic plasma parameters, turbulence, and transport are examined. Turbulence measurements over a broad range in wavenumber ( $1\text{--}39\text{ cm}^{-1}$ ,  $k\rho_s = 0.1\text{--}10$ ) from multiple scattering diagnostics are presented. The measurements cover this wavenumber range with a significantly higher number of wavenumber points than previously reported on DIII-D due to upgraded and new diagnostic systems. In general, the density turbulence increases during ECH over the range of wavenumbers studied. The plasma parameter most affected by the ECH is the electron temperature, with the electron density and ion temperature roughly unchanged. Various stability parameters (e.g.  $T_e/T_i$ , scale lengths, etc.) are found to vary with ECH. Spatially resolved measurements of high  $k$  ( $k = 39\text{ cm}^{-1}$ ) turbulence show a varying spatial response to ECH heating, decreasing at  $r/a = 0.35$  and

increasing at  $r/a = 0.6$  and 1. These variations were found to have a positive correlation with  $\nabla T_e$  from nearby locations consistent with a  $\nabla T_e$  drive. Gyrokinetic stability calculations using the GKS code [12] are performed using the measured plasma parameters. Comparison of the changes in high  $k$  fluctuation levels to linear gyrokinetic growth rates show qualitative agreement at the innermost location,  $r/a = 0.35$  and disagreement at  $r/a = 0.6$ .

## 2. Experimental Results

The experiments described here were performed on a lower single-null, diverted, sawtoothed DIII-D discharge. The plasma parameters were  $B_T = 2.1$  T,  $I_p = 0.75$  MA, line averaged density  $n_e = 1.8 \times 10^{19} \text{ m}^{-3}$ , and deuterium working gas. A moderate amount of 110 GHz ECH (1.4 MW) was applied to these Ohmic discharges during the plasma current flat top (figure 1). The heating location was located near normalized radial location  $\rho \approx 0.6$ , with a heating deposition width of approximately  $\pm 0.1$  in normalized radial units. The density was well controlled during this time period by feedback control of the gas puff using the  $\text{CO}_2$  interferometer signal (figure 1). Short duration neutral beam blips (10 ms) were injected at different times on repeat shots to obtain carbon ion temperature and density information from charge exchange recombination (CER). The major change to the plasma due to the ECH was an increase in the electron temperature (figure 1). The analysis focuses on two times during these discharges, the Ohmic time period at 1800 ms and the ECH time period at 3465 ms. Based upon the time histories of the various plasma parameters these times appear quite stationary. The plasmas examined here have some similarities to the plasma described in the first part of reference [7] but also some striking differences. The similarities are principally that both are Ohmic plasmas with auxiliary ECH heating. The major qualitative differences are lower ECH power for the plasmas herein ( $\sim 1.4$  MW compared to  $\sim 2.4$  MW in [7]) and the operational difference that the plasma density was allowed to decrease in [7] whereas it was kept relatively constant here [e.g. figure 1(a)]. Other, more quantitative differences will be discussed later. In addition to these differences a much improved fluctuation data

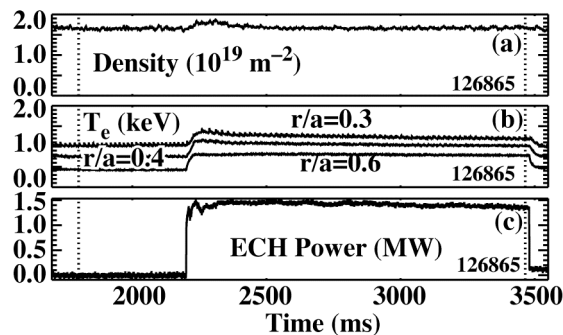


**Figure 1.** Time histories of (a) line averaged electron density from a  $\text{CO}_2$  interferometer, (b) electron temperature from ECE and (c) electron cyclotron heating power (heating location  $\rho = 0.6$ ).

set was obtained for the plasmas reported upon here. This improved fluctuation data set consists of a larger number of monitored wavenumbers enabled by upgraded and new diagnostic systems.

Profiles of electron and ion temperatures, electron density, and magnetic safety factor  $q$  for the two times of interest are shown in figure 2. The electron temperature is obtained from a combination of multipoint Thomson scattering and electron cyclotron emission and shows the largest change due to the ECH. The ECH deposition (as determined by the TORAY code) is indicated by the shaded region in figure 2(a). Note that although the ECH is applied at normalized radial location  $\rho = 0.6$  the electron temperature increases significantly inside of this location possibly indicating an inward thermal transport. This phenomenon has been previously reported upon in various machines [13-16] and was concluded to be inconsistent with purely diffusive transport. The ion temperature is obtained from charge exchange recombination measuring the fully stripped carbon impurity. Electron density is obtained from a combination of Thomson scattering and density profile reflectometry. The magnetic safety factor  $q$  is obtained using the magnetic equilibrium code EFIT [17] constrained by motional Stark effect (MSE) measurements of the on-axis magnetic field [18]. The error bar analysis is based on multiple automatic spline fits to the data and indicate the one sigma error bar from the resulting distribution. For each fit the data are randomly varied within the measurement error and the profile refitted.

The parameters (other than  $T_e$ ) show little variation with the possible exception of the electron density at the edge that does show a small increase with ECH. In contrast to this, the inverse scale lengths ( $a/L_n$ ,  $a/L_{Te}$ ,  $a/L_{Ti}$ ) do vary with the addition of ECH with the largest changes in  $a/L_{Te}$  being found in the deep core while  $a/L_n$ , and  $a/L_{Ti}$  vary both towards the edge and in the core. Here  $a = 0.65$  m is the minor radius of the plasma on the outboard midplane and the scale lengths are calculated using  $L_Y = Y/(dY/dr)$ , where  $Y$  is  $T_e$ ,  $T_i$ ,  $n_e$ , etc. Interestingly, the inverse electron temperature scale length  $a/L_{Te}$  decreases during ECH indicating that the increase in  $T_e$  is larger than the increase in  $\nabla T_e$ . The magnetic safety factor  $q$  and the magnetic shear  $\hat{s} = (r/q)(\partial q/\partial r)$  do not vary significantly with ECH [figure 2(d,i)].  $Z_{\text{eff}}$  is approximately constant in radius with a value of  $1.25 \pm 0.1$  (calculated from charge balance using the measured electron density and the fully stripped carbon impurity density from CER) and did not change appreciably with ECH. These parameters, as well as those derived directly from them (e.g.  $T_e/T_i$ , collisionality, etc.) enter directly into stability calculations of the various modes believed responsible for anomalous plasma transport (e.g. ITG, ETG, TEM) [12,19-21].

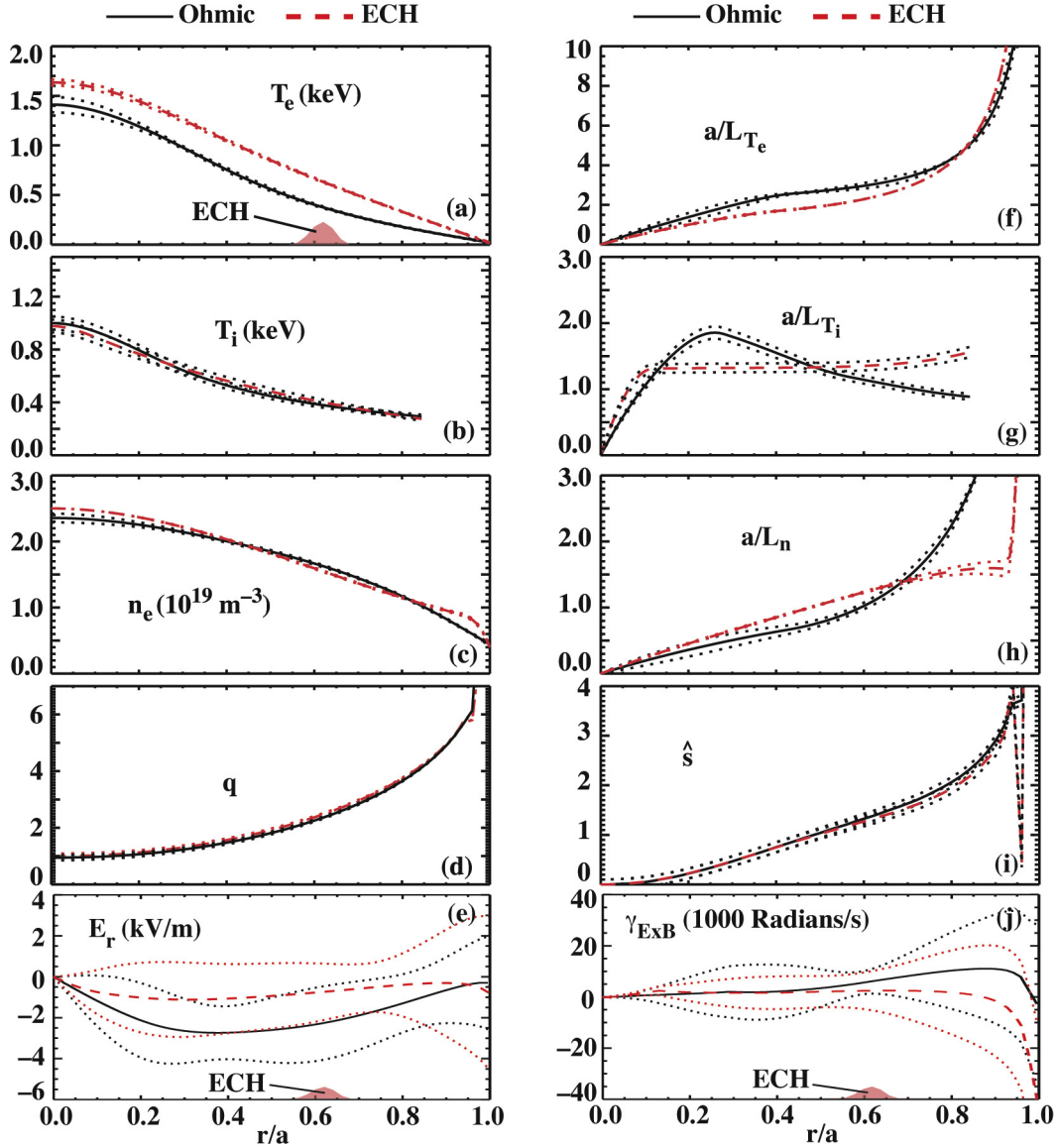


**Figure 2.** Profiles at 1800 ms Ohmic (solid line) and 3465 ms ECH (dashed line). (a)  $T_e$  from multipoint Thomson scattering and ECE, (b)  $T_i$  from CER, (c) electron density from multipoint Thomson scattering and profile reflectometry, (d) magnetic safety factor  $q$  and (e) radial electric field. The corresponding inverse scale lengths are shown in (f) through (h), (i) is the magnetic shear  $\hat{s} = (r/q)(\partial q/\partial r)$  and (j) the shearing rate of the radial electric field. Representative uncertainties are indicated by the dotted lines. The normalization factor  $a$  is 0.754 m in Ohmic and 0.755 m in ECH.

The radial electric field  $E_r$  and its radial shearing rate  $\gamma_{E \times B} = \left[ (RB_\theta)^2 / B \right] \times (\partial/\partial\psi)(E_r/RB_\theta)$  at these two times are shown in figure 2(e,j) (here  $R$  is major radius,  $B_\theta$  and  $B$  are the poloidal and total magnetic fields, and  $\psi$  is the poloidal flux representing the radial coordinate). The radial electric field is determined from the force balance equation using CER measurements of the fully stripped carbon temperature, density, and vertical and tangential velocities [22]. The radial electric field  $E_r$  and its

radial shearing rate  $\gamma_{E \times B}$  do appear to decrease on average with the application of ECH. However, within the uncertainties there is no clear difference between the two times of interest. Additionally, the magnitude of the shearing rate  $\gamma_{E \times B}$  is quite low at both times (especially in relation to the growth rates of the various plasma instabilities as will be seen later).

Thermal fluxes and diffusivities were calculated by the ONETWO transport code [23] using the measured profiles (figure 3) and the ECH power deposition (ECH deposition is from TORAY rf absorption code using measured profiles, magnetic equilibrium, ray tracing, etc.) location ( $r/a \sim 0.6$ ). Thermal diffusivities are of interest as they indicate how fast the plasma transports thermal energy whereas thermal fluxes are of interest since they are most directly related to the turbulent fluxes through standard flux relations, e.g. the turbulence induced diffusive heat flux  $\tilde{q}_e = n \langle \tilde{T}_e \tilde{E}_\theta \rangle / B \propto n k_\theta T_e^2 (\tilde{n}/n)^2 / B$ . Two different times are shown in figure 3 corresponding to no ECH ( $t = 1800$  ms) and 1.4 MW of ECH power ( $t = 3465$  ms). The ECH deposition location is indicated by the shaded region. Both thermal fluxes and diffusivities increase with ECH for radii outside of the ECH deposition location while both decrease for  $r/a < 0.6$ . The decrease inside of  $r/a \sim 0.6$  is a manifestation of the phenomenon discussed earlier (and reported in [13]) where, although the ECH is deposited locally at  $r/a \sim 0.6 \pm 0.1$ , the electron temperature increases interior to the heating - even though the temperature gradient is negative in that region (i.e. the diffusive transport should be down gradient). The diffusivities are well above the neo-classical ion diffusivities with the exception of the very core,  $r/a < 0.15$ .

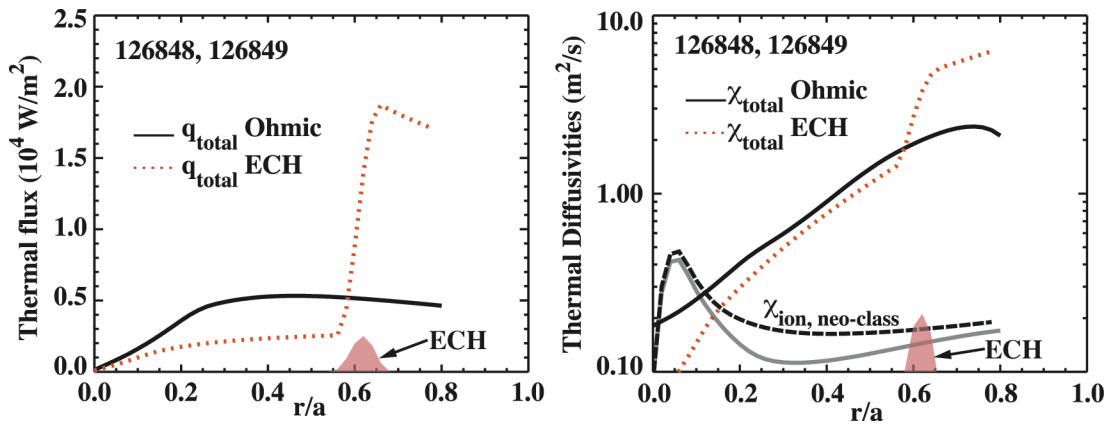


**Figure 3.** Single fluid (a) thermal fluxes and (b) diffusivities at 1800 ms (Ohmic) and 3465 ms (ECH). The neoclassical ion diffusivities are shown in (b) for reference.

The response of the turbulent density fluctuations was measured over a broad wavenumber range using a combination of FIR scattering and mm-wave backscattering diagnostics [6]. FIR scattering was utilized to monitor the wavenumber ranges  $1 \text{ cm}^{-1}$

[figure 4(a)] and  $8\text{--}15\text{ cm}^{-1}$  [figure 4(b-d)]. A scan of the intermediate wavenumber range  $8\text{--}15\text{ cm}^{-1}$  was obtained by scanning the receiver angle (proportional to the detected wavenumber) on reproducible shots. The FIR scattering diagnostic is aligned along the tokamak midplane and principally detects fluctuations with a poloidal wavenumber in the region near the midplane. The instrument function for these wavenumbers is quite broad in real space, being approximately the full diameter of the plasma for  $1\text{ cm}^{-1}$  and the minor radius for  $8\text{--}15\text{ cm}^{-1}$ . The FIR scattering system measures the fluctuations in the laboratory frame of reference, including both intrinsic fluctuation frequency and any  $E \times B$  Doppler frequency shift that may be present [24,25]. The spatial variation of the combined intrinsic fluctuation frequency and the  $E \times B$  Doppler frequency shift has been utilized to improve the spatial resolution of similar measurements [25]. In this picture higher measured frequencies are mapped to regions of larger total frequency that typically occur towards the mid-radius of the tokamak (the total measured frequency being the sum of the intrinsic fluctuation frequency and  $E \times B$  Doppler frequency shift). This prescription gives rise to ambiguities since low Doppler shift frequencies can occur at both the edge and  $r/a=0$ . This ambiguity is partially resolved by noting that fluctuation levels generally peak towards the edge. Thus, the edge region will tend to dominate the low frequency part of the FIR power spectrum.

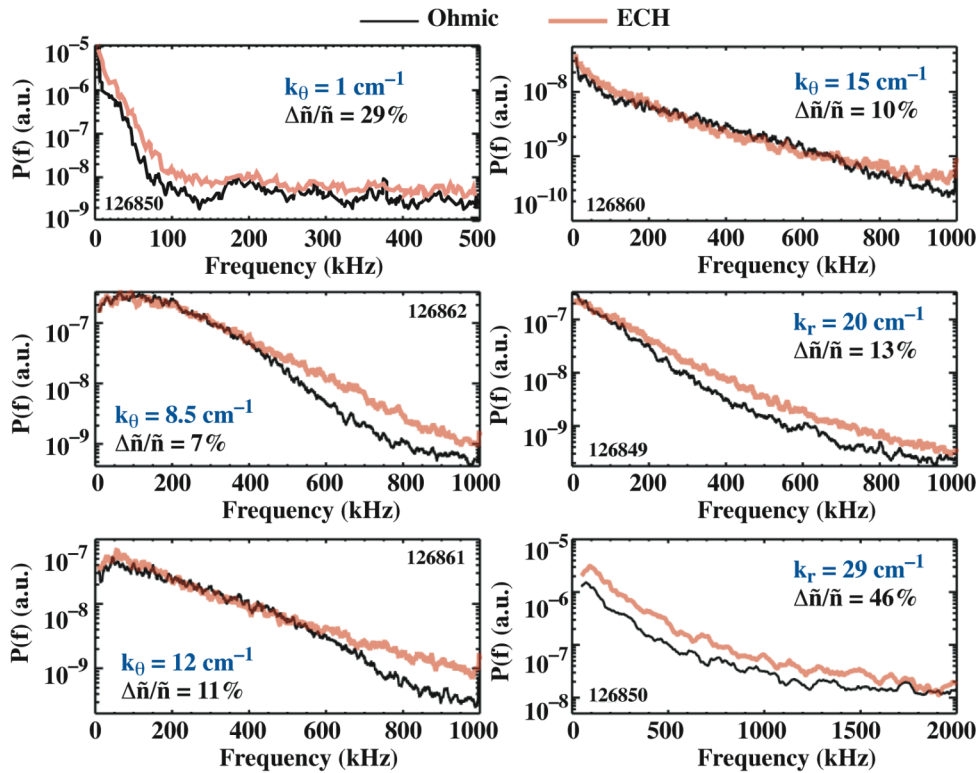


**Figure 4.** Power spectra ( $\tilde{n}^2$ ) for  $k =$  (a)  $1\text{ cm}^{-1}$ , (b)  $8.2\text{ cm}^{-1}$ , (c)  $12\text{ cm}^{-1}$ , (d)  $15\text{ cm}^{-1}$ , (e)  $20\text{ cm}^{-1}$ , and (f)  $39\text{ cm}^{-1}$  for 1800 ms Ohmic (black) and 3465 ms ECH (red).

For the higher wavenumbers,  $k \geq 20 \text{ cm}^{-1}$ , two channels of mm-wave backscattering are utilized. One channel detects  $\sim 20 \text{ cm}^{-1}$  and integrates from the edge plasma inward to approximately  $r/a = 0.2$  [figure 4(e)]. A second channel detects  $\sim 39 \text{ cm}^{-1}$  and also integrates from the edge plasma inward to approximately  $r/a = 0.3$  [figure 4(f)]. A more complete description of the backscattering diagnostic can be found in [6,7]. These backscattering channels principally measure radial  $k$  and so are different from the FIR scattering in that respect.

For reference, the density wavenumber ranges in terms of normalized wavenumber,  $k\rho_s$  ( $\rho_s$  is the ion gyroradius using the local electron temperature) are  $k\rho_s \sim 0.1\text{--}0.3$  for  $1 \text{ cm}^{-1}$ ,  $k\rho_s \sim 0.8\text{--}2.5$  for  $8.2 \text{ cm}^{-1}$ ,  $k\rho_s \sim 1.2\text{--}3.6$  for  $12 \text{ cm}^{-1}$ ,  $k\rho_s \sim 1.5\text{--}4.5$  for  $15 \text{ cm}^{-1}$ ,  $k\rho_s \sim 2\text{--}6$  for  $20 \text{ cm}^{-1}$ ,  $k\rho_s \sim 4\text{--}12$  for  $39 \text{ cm}^{-1}$ . Here we have used values of the gyroradius ( $\rho_s = 0.1\text{--}0.3 \text{ cm}$ ) representing both the variation of  $\rho_s$  with ECH as well as its spatial variation. This provides a total variation in  $k\rho_s$  of approximately 0.1–12. This range in wavenumber is typically associated with ITG driven modes ( $k\rho_s$  roughly 0.1–0.5), TEM ( $k\rho_s \sim 0.5$  to 2 or greater), and ETG driven modes ( $k\rho_s \sim 2$  and larger).

The fluctuation spectra shown in figure 4 are broad and generally featureless with the exception of the  $k = 8.2$  and  $12 \text{ cm}^{-1}$  [figure 4(b,c)] data which show a rather wide low frequency peak. These plasmas were relatively free of MHD type activity and this is reflected in the lack of coherent modes in the fluctuation data. In all these cases the total fluctuation level  $\tilde{n}$  (integrated over the individual frequency ranges shown) increases with ECH (the percentage change in  $\tilde{n}$  is indicated in each figure). Note that this  $\tilde{n}$  is not a normalized level (i.e. it is not  $\tilde{n}/n$ ). The increase is not a constant change over each frequency range but instead can be somewhat complicated. For example, the change in the  $k = 12 \text{ cm}^{-1}$  data [figure 4(c)] occurs principally at low and high frequencies with the intermediate frequency range showing little variation. In contrast, the data for  $k = 8.2 \text{ cm}^{-1}$  [figure 4(b)] shows an increase at the higher frequencies only. This variation with frequency is likely due to the spatial variation of the fluctuation level that is mapped onto the measured frequency as discussed above. The highest  $k$  channel [figure 4(f)] shows an increase at all frequencies up to the point that the instrument noise floor is reached.

Data from a second channel of high- $k$  at  $\sim 39 \text{ cm}^{-1}$  with much better spatial localization ( $\sim \pm 0.1$  in  $r/a$ ) were also obtained on these discharges (figure 5). The spatial location was varied shot to shot covering  $r/a = 1 \pm 0.1$ ,  $r/a = 0.6 \pm 0.1$ , and  $r/a = 0.35 \pm 0.1$ . This spatial localization is accomplished by crossing a probe beam and a detection beam at an angle of  $\sim 12$  deg and is discussed in more detail in [7]. The index of refraction

slightly modifies the local wavenumber  $k$  of the probe beam (maximum is 10% at the innermost position) according to  $k = Nk_0$ , where  $k_0$  is the vacuum wavenumber and  $N$  is the local index of refraction. The approximate local value of the wavenumber is indicated in the caption of figure 5. Power spectra vs. frequency from these three radial locations are shown in figure 5 for both the Ohmic and ECH times. The percentage change in fluctuation level comparing ECH to Ohmic is indicated in each panel. Notably the fluctuation level *decreases* at the innermost location,  $r/a = 0.35$ , while it increases outside of that. The changes in level also vary with radius,  $\Delta\tilde{n}/\tilde{n} = -14\%$ ,  $+43\%$ , and  $+28\%$  for radial locations  $r/a = 0.35$ ,  $0.6$ , and  $1.0$ , respectively. The spectral width is also seen to increase significantly with radius. Since this diagnostic measures principally radial wavenumber, this spectral broadening is unlikely to be due to Doppler effects and is rather related to changes in the underlying turbulence spectrum.

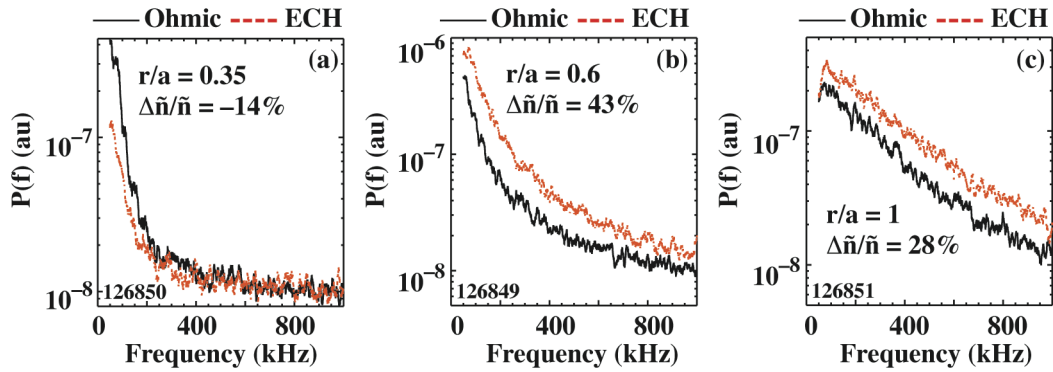


**Figure 5.** Spatially resolved high- $k$  fluctuation power spectra for the radial positions (a)  $r/a = 0.35$  ( $k = 35 \text{ cm}^{-1}$ ), (b)  $r/a = 0.6$  ( $k = 36 \text{ cm}^{-1}$ ), and (c)  $r/a = 1$  ( $k = 39 \text{ cm}^{-1}$ ) at 1800 ms Ohmic (black) and 3465 ms ECH (red).

Since the most significant change with ECH is in the electron temperature (figure 2) and since ETG type instabilities are driven by gradients in electron temperature it is natural to compare local changes in  $\nabla T_e$  to these measurements (figure 6). The innermost location ( $r/a = 0.35$ ) shows a clear correlation between the decreased  $\tilde{n}$  and decreased  $\nabla T_e$  during ECH. The outermost location ( $r/a = 1$ ) also shows a correlation with increased  $\tilde{n}$  and increased  $\nabla T_e$ . The correlation at this location is not as clear since  $\nabla T_e$  is obtained from ECE measurements at  $r/a = 0.76$ . For comparison the gradient obtained from Thomson scattering (at much lower time resolution) near  $r/a \sim 1$  is shown. The  $r/a = 0.6$  position indicates a more complicated picture, with the  $\tilde{n}$  positively correlated with the  $\nabla T_e$  at  $r/a \sim 0.63$ . However, within the fluctuation measurement volume  $\nabla T_e$  both increases and decreases as shown in figure 6(d). Thus, the response of the high  $k$   $\tilde{n}$  is likely due to an integral over a region where the fluctuation levels both increase and decrease. It is also noteworthy that all locations show an *increase* in  $\tilde{n}$  with NBI

injection ( $\sim 3700\text{--}3800$  ms in figure 6) in contrast to the behavior with ECH. Examination of figure 6(b) shows that this behavior is consistent with local changes in  $\nabla T_e$  just as in the ECH time period.

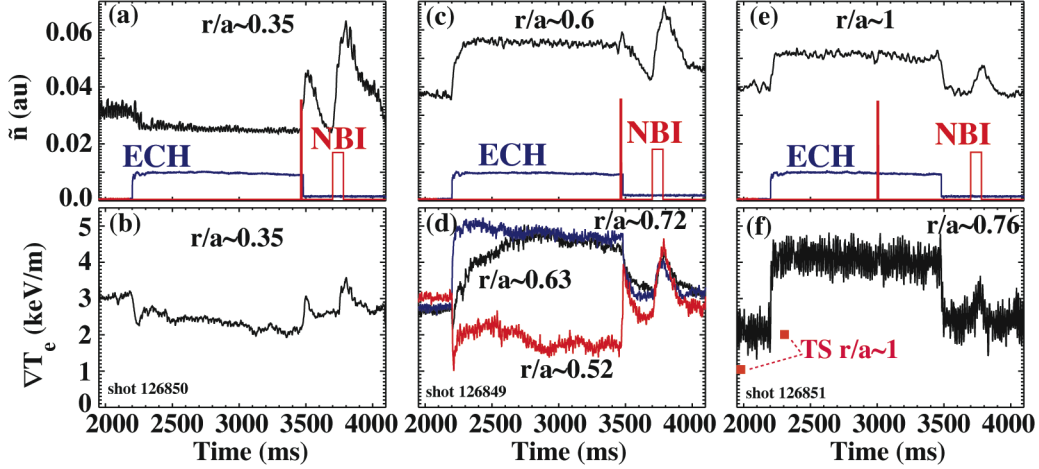


**Figure 6.** Comparing high- $k$  ( $k \approx 39 \text{ cm}^{-1}$ )  $\tilde{n}$  RMS fluctuation levels (a,c,e) to local temperature gradients (b,d,f) from ECE measurements at the three different radial locations shown.

As mentioned earlier, these plasmas show some similarity to those presented in the first part of reference [7] with some striking and important differences. The density profile was approximately constant here while it varied in [7]. The radial electric field and shear were both low and unchanged within error bars in contrast to the variation in  $E_r$  and, significantly, the increase in electric field shear reported in [7]. These differences are attributed to a combination of lower ECH power and, possibly more importantly, the relatively constant density that was obtained in these plasmas. The fluctuation data presented in this paper covers the same total range in wavenumber space but with a much larger number of monitored wavenumbers. The fluctuation levels are found to increase at all wavenumbers (with the exception of the high  $k$  at  $r/a = 0.35$ ) whereas those in [7] increased only at the highest  $k$ . In [7] the lack of change at lower wavenumbers was attributed to the increase in electric field shear offsetting the increase in calculated growth rates. Given that the electric field shear did not change appreciably, the increase in lower  $k$  fluctuations here is consistent with the picture developed in [7].

### 3. Comparison with Linear Gyrokinetic Calculations

Comparisons of the above data to linear gyrokinetic simulations were performed using the GKS code [12]. GKS is a gyrokinetic stability code, which calculates linear growth rates and frequencies for toroidal drift waves corresponding to poloidal wavenumbers. Code inputs were the measured  $T_e$ ,  $T_i$ ,  $n_e$ , impurity profiles (assuming that the fully stripped carbon is the major impurity), and magnetic equilibrium (the profiles used are shown in figure 2). The effects due to up-down plasma asymmetries or  $E \times B$  velocity shear flow ( $E$  and  $B$  are local electric and magnetic fields) are not included in GKS. Linear calculations do not simulate the fully developed turbulence but they can provide a guide as to where particular instabilities might appear. The GKS code calculates poloidal wavenumber characteristics, however the mm-wave backscatter data [ $k = 20$  and  $39 \text{ cm}^{-1}$ , figures 4(e,f), 5 and 6] are principally radial  $k$  (as contrasted with the FIR scattering which is principally  $k_\theta$ ).

The results of the GKS simulations are shown in figure 7, which shows growth rates and real frequencies for the radial locations  $r/a = 0.36$  and  $0.6$ . The convention used in GKS is that positive growth rates indicate instability. Positive and negative frequencies correspond to propagation of the instability in the electron and ion diamagnetic drift directions respectively. During the Ohmic time period both radial locations indicate instabilities over the range  $k_\theta \rho_s$  from 0.1 to 10, which encompasses the ITG-TEM-ETG wavenumber ranges. The real frequency plots [figure 7(c,d)] indicate ion type modes at lower  $k_\theta \rho_s$  that change to electron type modes as  $k_\theta \rho_s$  increases. During ECH the range  $k_\theta \rho_s = 1-10$  changes markedly at  $r/a = 0.36$ . In the region  $k_\theta \rho_s > 1$  [figure 7(a)] the growth rates decrease to  $\leq 0$  indicating that these wavenumbers are no longer linearly unstable (note that on the log plot these values are not plotted). Interestingly, there is little change in the growth rates for  $k_\theta \rho_s < 1$  and there the real frequencies remain in the ion direction. This decrease in the high  $k$  growth rates is qualitatively consistent with the decrease in high  $k \tilde{n}$  shown in figures 5(a) and 6(a). Quantitatively, there is less agreement at this location since the measured fluctuation levels are not completely suppressed.

The electron temperatures and scale lengths were varied in the calculation in order to address what parameter is most responsible for the stabilization of the high  $k$ . Note that these variations can only be consistently performed at one point, in this case  $r/a = 0.36$ . The curve marked (1) in figure 7(a) is the growth rate using the electron temperature

during ECH but increasing  $a/L_{Te}$  to near the Ohmic level [e.g. figure 2(f)]. The resulting growth rate becomes non-zero and increases to above the Ohmic level for  $k_{\theta}\rho_s > 1$ . Curve (2) in figure 7(a) shows the result of reducing the local  $T_e$  to near the Ohmic value but keeping  $a/L_{Te}$  close to the ECH value. Interestingly the growth rate also becomes non-zero for  $k_{\theta}\rho_s > 1$  and but does not increase as much as curve (1). Also, there are regions that are still stable (e.g. around  $k_{\theta}\rho_s = 1$ , and above. From this it is concluded that both  $T_e$  and  $a/L_{Te}$  affect the calculated stability with  $a/L_{Te}$  having the largest effect. This is consistent with the strong correlation between  $\tilde{n}$  and  $\nabla T_e$  shown in figure 6(a). Figure 7(b) is the corresponding GKS calculation for  $r/a = 0.6$  and indicates that the high  $k$  growth rate  $k_{\theta}\rho_s > 1$  decreases with ECH but remains far above zero. This is qualitatively inconsistent with the increased fluctuation level at that radius shown in figures 5(b) and 6(c). GKS calculations out to  $r/a = 0.7$  also show a decrease in this wavenumber range during ECH indicating that the discrepancy cannot be resolved by invoking the spatial integration volume of the measurement.

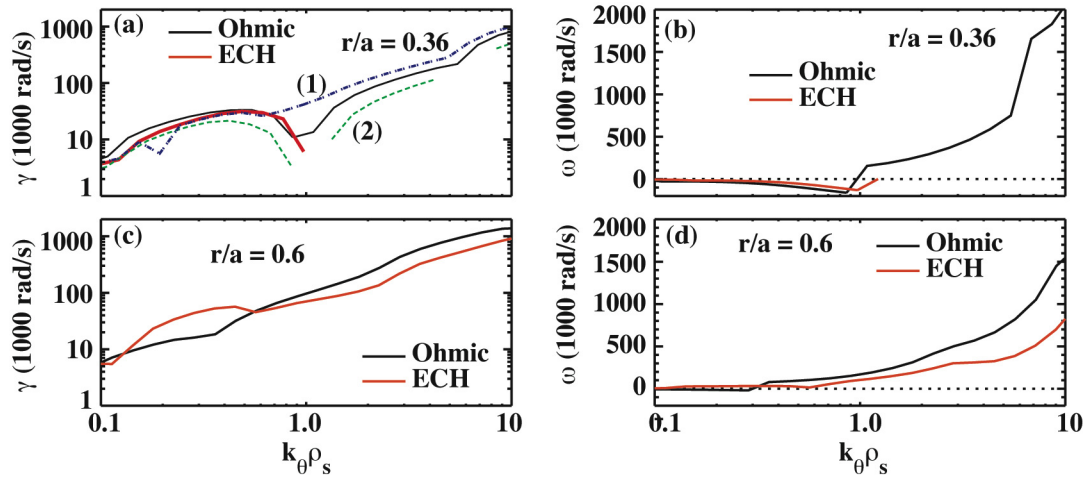


**Figure 7.** GKS calculations of linear growth rates, (a) and (c), and real frequencies, (b) and (d) at the radial locations  $r/a = 0.36$  and  $0.6$  for the Ohmic (black solid) and ECH (red solid) times. The marked curves are growth rates calculated with (1)  $T_e$  from the ECH time and  $a/L_{Te}$  near the Ohmic value and (2)  $T_e$  near the Ohmic value and  $a/L_{Te}$  from the ECH time period. The measurement region of the high  $k$  diagnostic is approximately  $k\rho_s = 7-8$  in (a) and (b),  $k\rho_s = 6-7$  in (c) and (d).

The increased electric field shear reported in [7] was conjectured to be the underlying cause of the lack of increase in measured lower  $k$  fluctuation levels as compared to the predicted increase. The data presented here appear to be consistent with that picture since the fluctuations increase in a broadband manner similar to calculated growth rates while at the same time there is no strong variation in  $E_T$  shear [it may in fact decrease, figure 2(j)]. However, it is noted that the lack of  $T_i$  for  $r/a > 0.85$  precludes linear stability calculations for  $r/a > 0.85$  in the plasmas reported upon here. Nevertheless, the

increase in  $T_e$  with ECH will tend to increase the ITG instability drive consistent with the increased low  $k$  fluctuation levels reported here.

Calculations of the critical gradient for ETG were also performed using GKS. These showed that during the Ohmic time period the plasma region  $r/a > 0.3$  is unstable to ETG modes. With ECH, this unstable region shifts outward to  $r/a > 0.4$ . This is consistent with the calculations shown in figure 7. In both Ohmic and ECH cases, the amount by which experimental gradient exceeds the critical gradient increases with increasing  $r/a$ . This is indicative of a stronger level of ETG drive which in turn implies larger levels of ETG fluctuations towards the edge. Future work will address this radial distribution.



## 4. Summary and Conclusions

In order to better understand plasma turbulence and the resulting transport, selected plasmas were perturbed in a controlled manner while measuring a range of turbulence wavenumbers and plasma parameters. Electron cyclotron heating was injected into a diverted, Ohmic DIII-D discharge and the plasma response measured. The density was well controlled and the resulting change to the gross plasma parameters was limited mainly to the electron temperature. Turbulence levels over a broad wavenumber range increased significantly during ECH as did the single fluid thermal flux and diffusivity. Interestingly, spatially localized measurements of high  $k$  fluctuation levels ( $k = 39 \text{ cm}^{-1}$ ) show a varying spatial behavior in response to ECH heating, decreasing at  $r/a = 0.35$  and increasing at  $r/a = 0.6$  and  $1$ . These variations were found to have a positive correlation with the  $\nabla T_e$  evaluated at nearby locations, consistent with a  $\nabla T_e$  drive. Comparison to linear gyrokinetic growth rates (from GKS) show qualitative agreement with the high  $k$  measurement at the innermost location,  $r/a = 0.35$ . Quantitatively, the measurement showed a non-zero fluctuation level during ECH in contrast to the predicted stabilization of high  $k$ . The changes due to ECH in calculated high  $k$  growth rates at  $r/a = 0.35$  were primarily due to changes in the electron temperature scale length and, to a lesser extent, changes in  $T_e$ . The decrease in linear growth rates with ECH calculated for  $r/a = 0.6$  appear to be in contradiction to the measured increase in high  $k$  fluctuation levels there. Nonlinear or non-local effects in fully developed turbulence may hold the key to this discrepancy.

From an operational point of view these types of plasma perturbations are quite useful as they result in changes to principally one parameter, in this case the electron temperature. The resulting changes in the various turbulence related stability parameters (e.g.  $a/L_n$ ,  $a/L_{Te}$ ,  $a/L_{Ti}$ , etc.) were more varied. In particular, the variation in  $a/L_{Ti}$  was larger than one would like. Nevertheless, by measuring the relevant parameters significant comparisons to theory and simulation can be performed. Future experiments will seek to further separate and clarify the interactions and dependence between the low  $k$  and high  $k$  turbulence.



## References

- [1] Carreras B A 1997 IEEE Trans. Plasma Sci. **25** 1281
- [2] Horton W, 1999 Rev. Mod. Phys. **71**, 735
- [3] Holland C and Diamond P H 2004 Phys. Plasmas **11** 1043
- [4] Candy J and Waltz R E 2007 Fusion Energy 2006 (Proc. 21st Int. Conf. Chengdu, 2006) (Vienna: IAEA) CD-ROM file TH/2-1 and <http://www-naweb.iaea.org/naweb/physics/FEC/FEC2006/html/index.htm>
- [5] Waltz R E, Candy J and Fahey M 2007 Phys. Plasmas **14** 056116
- [6] Rhodes T L *et al* 2006 Rev. Sci. Instrum. **77** 10E922
- [7] Rhodes T L *et al* 2007 Phys. Plasmas **14** 056117
- [8] Gusakov E Z *et al* 2006 Plasma Phys. Control. Fusion **48** A371–A376
- [9] Gusakov E Z *et al* 2006 Fusion Energy 2006 (Proc. 21st Int. Conf. Chengdu, 2006) (Vienna: IAEA) CD-ROM file EX\_P4-32 and <http://www-naweb.iaea.org/naweb/physics/FEC/FEC2006/html/index.htm>
- [10] Hennequin P *et al* 2004 Plasma Phys. Control. Fusion **46** B121
- [11] Kaye S M *et al* 2006 Fusion Energy 2006 (Proc. 21st Int. Conf. Chengdu, 2006) (Vienna: IAEA) CD-ROM file EX-8-6 and <http://www-naweb.iaea.org/naweb/physics/FEC/FEC2006/html/index.htm>
- [12] Kotschenreuther M, Rewoldt G W and Tang W M, 1995 Comput. Phys. Commun. **88** 128
- [13] Luce T C, Petty C C, de Haas J C M 1992 Phys. Rev. Lett. **68** 52
- [14] Mantica P *et al* 2006 Plasma Phys. Control. Fusion **48** 385
- [15] Sozzi C *et al* 2000 *18th IAEA Fusion Energy Conf. (Sorrento)* exp 5-13
- [16] Mantica P *et al* 2000 Phys. Rev. Lett. **85** 4534
- [17] Lao L L *et al* 2005 Fusion Sci. Tech. **48** 968
- [18] Holcomb C T *et al* 2006 Rev. Sci. Instrum. **77** 10E506
- [19] Weiland A, Jarmen B and Nordman H 1989 Nucl. Fusion **29** 1810
- [20] Davydova T A, Weiland J and Yakimenko A I 2002 Phys. Plasmas **9** 4623
- [21] Dong J Q, Horton W and Kim J Y 1992 Phys. Fluids B **4** 1867
- [22] Burrell K H 1997 Phys. Plasmas **4** 1499
- [23] St John H E, Taylor T S, Lin-Liu Y R and Turnbull A D 1994 Plasma Phys. Control. Nucl. Fusion Research **3** 603
- [24] Koch R A and Tang W M 1978 Phys. Fluids **21** 1236
- [25] Philipona R *et al* 1993 Phys. Fluids B **5** 87



## **Acknowledgments**

This work was supported by the U.S. Department of Energy under DE-FG03-01ER54615, DE-FG03-97ER54415, DE-FC02-04ER54698, W-7405-ENG-48, and DE-AC02-76CH03073. Helpful discussions with Dr. R.E. Waltz, General Atomics, are acknowledged.